

Fundamental Bounds for Off-Axis Illumination in Interferometric and Rotating Coherent Scattering Microscopy

Felix Hitzelhammer ,¹ Jonathan Dong ,² Ulrich Hohenester ,¹ and Thomas Juffmann ,^{3,4}

¹*Institute of Physics, NAWI Graz, University of Graz, 8010 Graz, Austria**

²*Biomedical Imaging Group, École polytechnique fédérale de Lausanne, 1015 Lausanne, Switzerland*

³*Faculty of Physics, VCQ, University of Vienna, 1090 Vienna, Austria*

⁴*Max Perutz Labs, University of Vienna, 1030 Vienna, Austria*

(Dated: October 6, 2025)

Coherent localization microscopy enables three-dimensional localization with nanoscale precision. Previous studies have characterized the fundamental precision limits for on-axis illumination geometries. In this paper, we theoretically analyze 3D particle localization precision under oblique illumination in interferometric scattering microscopy (iSCAT). We show that (quantum) Cramér-Rao bounds reveal an information gain in the off-axis case, potentially enabling enhanced localization precision. We find that rotating coherent scattering microscopy (ROCS), which employs off-axis illumination, provides worse localization precision than iSCAT, despite offering higher spatial resolution. This shows that key metrics, like spatial resolution, are often insufficient to fully characterize a microscopy technique.

Elastic light scattering underpins diverse applications, from mass photometry [1] to fast particle tracking [2] and 3D imaging [3]. A prominent technique is interferometric scattering microscopy (iSCAT), which enhances contrast by interfering scattered light with a reference field from the partial reflection of wide-field incident illumination [4]. For 3D imaging, this geometry is particularly sensitive for axial localization [5, 6]. Recent advances suggest that oblique illumination can improve interferometric imaging. A key example is rotating coherent scattering microscopy (ROCS) [7–9], where the angle of incidence rotates around the optical axis. ROCS offers higher spatial resolution and contrast than on-axis schemes.

In coherent imaging, measurement precision is limited by shot noise, i.e., quantum fluctuations in detected photons. While collecting more photons increases precision, this is constrained by sample dynamics, camera well depth, photodamage, or setup stability. It is therefore crucial to maximize the information extracted per photon. Two quantities capture this shot-noise-limited precision. The Fisher information (FI) quantifies how much information Poisson-distributed measurements carry about a parameter [10, 11], and is bounded above by the quantum Fisher information (QFI), which describes the information in the quantum state of the scattered light [12]. Their inverses define the Cramér-Rao bound (CRB) and quantum Cramér-Rao bound (QCRB), which set limits on localization precision based on the noisy measurements, or based on the quantum state itself, respectively.

Previous work [6] computed FI and QFI in conventional iSCAT at normal incidence, revealing a drastic difference between axial and transverse localization. However, the off-axis case remains unexplored, as it requires modeling of non-paraxial field propagation and of scat-

terer-interface couplings.

In this paper, we investigate how off-axis illumination affects localization precision in coherent scattering. Using a numerical toolbox for coherent imaging [13], we simulate electric fields and compute classical and quantum FI with associated CRBs. We first demonstrate how the spatial distribution of the FI flow [14] depends on illumination angle and numerical aperture (NA). We then show that oblique illumination increases the QFI of the scattered light and yields up to twofold improvements in transverse localization in iSCAT. Lastly, we analyze CRBs in ROCS, where, despite higher spatial resolution, localization precision is degraded.

Theory.—The detector intensity from the superposition of scattered and reflected fields is [15]

$$\begin{aligned} I^{(\theta, z_f)}(x, y) &= |\mathbf{E}_s e^{i\phi_s} + \mathbf{E}_r e^{i\phi_r}|^2 \\ &= |\mathbf{E}_s|^2 + |\mathbf{E}_r|^2 + 2 E_s E_r \cos \phi, \end{aligned} \quad (1)$$

with lateral coordinates (x, y) , incident angle θ , defocus z_f , and relative phase $\phi = \phi_s - \phi_r$. For brevity, the (x, y) -dependence is omitted on the right-hand side. The interferometric point-spread function (iPSF) under off-axis illumination is computed using a numerical toolbox [13] that combines the boundary element method for scattering fields [16, 17] with a vectorial high-NA imaging model [6, 18], where the focus field is expressed as a superposition of far fields $\epsilon(\Theta, \phi)$ over back-focal-plane coordinates (Θ, ϕ) . We compare our numerical results to an analytic simplified dipole model, denoted as dipole approximation, that uses the quasistatic approximation and models the nanosphere as a small polarizable sphere [5]. We then consider the far-fields of the resulting dipole emitter in the vicinity of the substrate (see Appendix D of [19]).

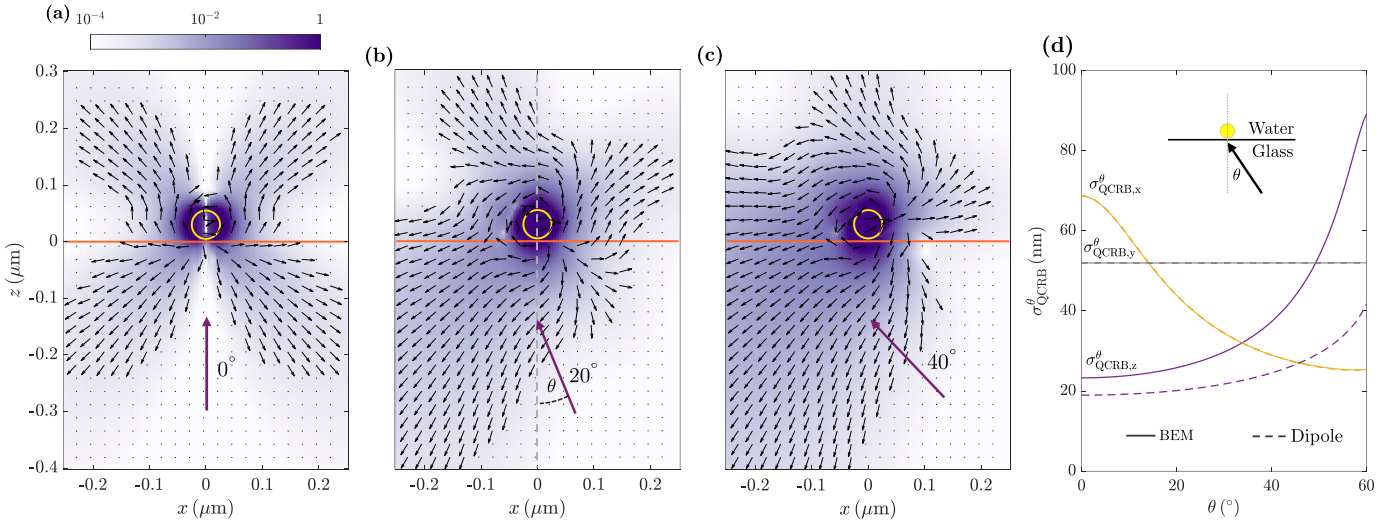


FIG. 1. Fisher information (FI) flow (a.u.) in the x - z plane for a gold nanosphere (golden circle) near a glass–water interface (orange line), together with the quantum Cramér-Rao bounds (QCRBs) for 3D localization precision under off-axis illumination. (a) FI flow under on-axis illumination, i.e. along the optical axis (gray dashed line). (b) FI flow for an illumination angle of 20°. (c) FI flow for an illumination angle of 40°. (d) QCRBs for localization precision along the x (orange line), y (grey line), and z (purple line) directions. Table 1 reports the measurement-independent gain in localization precision predicted by the QCRBs for off-axis illumination in panel (d).

The CRB sets a lower limit on the variance of any unbiased estimator $\hat{\gamma}$ [10]. In the many-photon limit the maximum likelihood estimator is unbiased and efficient, making the CRB directly relevant for localization precision in interferometric imaging. The CRB is given by the inverse of the FI, which quantifies the sensitivity of the data to changes in parameters [20]. We estimate the 3D localization precision for $\gamma = (x, y, z)$ using the FI matrix

$$[\mathcal{I}(\gamma)]_{ij} = \int_C dx dy \frac{[\partial_{\gamma_i} I^{(\theta, z_f)}(x, y)] [\partial_{\gamma_j} I^{(\theta, z_f)}(x, y)]}{I^{(\theta, z_f)}(x, y)}, \quad (2)$$

where C denotes the region of integration across the image plane. We note that the form of the FI matrix depends on the detection statistics, which here are Poissonian, corresponding to the shot-noise-limited regime [21]. Since only few parameters are estimated, the derivatives in Eq. (2) are computed via finite differences. The FI matrix bounds the variance component-wise [6, 21]

$$\text{Var}(\hat{\gamma}_j) \geq [\mathcal{I}^{-1}(\gamma)]_{jj} \geq \frac{1}{[\mathcal{I}(\gamma)]_{jj}}, \quad (3)$$

where the second inequality gives a weaker bound. This applies to localization precision when assessing the sensitivity of the iPSF to a single parameter γ_j , assuming all others are perfectly known. The corresponding CRB on the standard deviation is then given by

$$\sigma_{\text{CRB}, \gamma_j} = \frac{1}{\sqrt{[\mathcal{I}(\gamma)]_{jj}}}. \quad (4)$$

In contrast to the classical CRB, the QCRB is measurement-independent and thus provides the ultimate benchmark in evaluating the potential of an imaging geometry [11, 22]. In [12] an analytical expression of the QFI in the context of coherent scattering is derived, which is applicable to iSCAT where the scattered and reflected fields interfere coherently. Building on this, we use the representation of the scattered light as a superposition of coherent states with amplitudes $\epsilon(\Theta, \phi)$, leading to the following expression for the QFI [6]

$$\mathcal{K}_{jj} = 4 \int_0^\alpha d\Theta \int_0^{2\pi} d\phi |\partial_j \epsilon(\Theta, \phi)|^2, \quad (5)$$

where α is the maximal angular aperture of the objective. We again use finite differences to compute partial derivatives and normalize the state to one scattered photon going through the backfocal plane [6], i.e. $\int_0^\alpha d\Theta \int_0^{2\pi} d\phi |\epsilon(\Theta, \phi)|^2 = 1$. We can formulate a quantum counterpart to Eq. (4) as

$$\sigma_{\text{QCRB}, \gamma_j} = \frac{1}{\sqrt{\mathcal{K}_{jj}}}. \quad (6)$$

Recent work has introduced the flow of FI in electromagnetic scattering problems [14]. In the context of iSCAT, the FI flow regarding localization precision in the x -direction is given by

$$\mathbf{S}_x^{\text{FI}} = \frac{2}{\hbar\omega} \text{Re}\{\partial_x \mathbf{E}_{\text{sca}} \times \partial_x \mathbf{H}_{\text{sca}}^*\}, \quad (7)$$

where \mathbf{E}_{sca} , \mathbf{H}_{sca} denote the fields scattered by the particle and the derivatives ∂_x are taken with respect to the particle position.

Results.—All our simulations were performed with the NANOSEM toolbox, which is based on the boundary element method, and its add-on for interference scattering microscopy [13]. Since the scattered photons carry the information, we calculate the (Q)CRBs per scattered photon collected by the imaging system [6].

Figure 1(a–c) shows simulation results of the FI flow for a gold nanosphere near a glass–water interface under off-axis illumination. The particle, illuminated from below by a TM-polarized plane wave at 520 nm and angle θ relative to the optical axis z , acts as the source of the flow. For on-axis illumination ($\theta = 0$), Fig. 1(a) shows that the forward- and backward-scattered fields carry nearly equal information. The flow propagates at an angle with respect to the optical axis, highlighting the role of high-NA detection. With off-axis illumination, the flow redistributes and is enhanced in the backward direction, as revealed in Figs. 1(b) and (c), suggesting that more information can be collected in iSCAT, where the imaging objective gathers backscattered light.

We quantify this conjecture in Fig. 1(d), where the QCRBs for 3D localization precision as a function of the illumination angle θ are shown. The solid lines are obtained using the NANOSEM simulation toolbox, while the dashed lines are calculated within the dipole approximation. We observe that the QCRBs are strongly dependent on the illumination geometry. Specifically, we find that the QCRBs in the x -direction improve by a factor of ≈ 2.8 , that is, they decrease with illumination angle, while those in the y -direction remain almost constant. This is a consequence of the incoming beam being tilted in the x - z plane, leading to more information being collected about the x -coordinate, in agreement with Fig. 1(a–c). Interestingly, for z -localization precision, the QCRBs worsen at the glass–water interface, as shown in Fig. 1(d), but improve at the glass–air interface, as demonstrated in Appendix Fig. 5(d). The measurement-independent improvements achievable with oblique illumination are summarized in Table I. In both cases, Figs. 1(d) and 5(d) show that the full BEM calculation yields different results from the dipole approximation. This discrepancy is particularly evident in Fig. 5(d), where the dipole model predicts a peak at the critical angle that is absent in the BEM calculation. A closer analysis revealed that this difference arises from higher multipoles induced in the sphere near the glass substrate, which are neglected in the dipole approximation. We note that the discrepancy would be smaller for non-metallic nanospheres.

For on-axis illumination, the FI flow in Fig. 1(a) indicates that 3D localization precision depends strongly on the NA of the imaging system. This is confirmed in Fig. 2, which shows CRBs versus NA over a large defocus

range. As expected, in panels (a–c) the CRBs decrease with increasing NA, but the deterioration is only a factor of ≈ 2.3 when comparing NA = 0.5 to NA = 1.5 near $z_f = 0$ nm. This suggests the feasibility of low-cost iSCAT setups with modest NA, provided samples are sparse to minimize interference from nearby scatterers. We also note the excellent axial CRBs in Fig. 2(c), arising from the strong axial dependence of the iSCAT signal on the particle–substrate distance z_p [6].

We next analyze the behavior of the CRBs under variations of (θ, z_f) and (θ, z_p) , where z_f and z_p denote the focus plane and particle position, respectively. Figure 3(a–f) shows 3D localization CRBs at a glass–water interface for both parameter sets in an iSCAT geometry. In panels (a–c), the defocus plane is fixed at 1 μm (vertical dashed line) while z_p is varied, a configuration relevant to nanoparticle tracking on cell membranes. In panels (d–f), the particle is near the interface and z_f is varied. The localization precision in x improves with illumination angle, as shown in panels (a) and (d), consistent across the entire defocus and particle range. The improved QCRBs from Fig. 1(d) translate into improved CRBs in the iSCAT geometry, both for the glass–water interface in Fig. 3(a),(d) case and the glass–air interface case in Fig. 5. In contrast, $\sigma_{\text{CRB},y}^\theta$ worsens with increasing θ (b,e), and $\sigma_{\text{CRB},z}^\theta$ generally worsens at larger θ (c,f). For a glass–air interface, however, axial precision improves with θ , as shown in Appendix Fig. 5(c,d). Interestingly, although Brewster-angle illumination increases contrast [13], the CRBs in all three spatial directions exhibit local maxima, corresponding to reduced localization precision. This underscores that contrast alone is not a reliable indicator. Furthermore, by comparing optimal bounds for off-axis illumination, denoted by a cross in Fig. 3(d), with an on-axis geometry, we report an enhancement factor of ≈ 1.8 for x at the glass–water interface. A similar analysis versus particle position in Fig. 3(a) shows a gain of ≈ 1.9 in x . For clarity, Figs. 6(a) and (b) show these enhancements for the glass–water interface. For the glass–air interface in Fig. 5(c), the global minima (marked by crosses) correspond to an enhancement factor of ≈ 1.8 in z . Figures 6(c),(d) further show this gain across the entire defocus range.

At low illumination angles, the CRBs oscillate with z_f , as can be seen in Figs. 3(a–c) and 6, due to interference between scattered and reference light [6]. These oscillations disappear at higher angles. Similarly, on-axis CRBs oscillate with z_p , but vanish under oblique illumination. Off-axis illumination can thus enable more robust particle localization, while maintaining precision. This can be understood qualitatively by recognizing that, for on-axis and $z_p \approx z_f$, most FI is concentrated at the IPSF center, whose contrast oscillates rapidly with the phase between scattered and reflected light, leading to oscillations in the FI and CRBs [6]. When the particle is out of focus, FI shifts to the outer rings of the IPSF, which

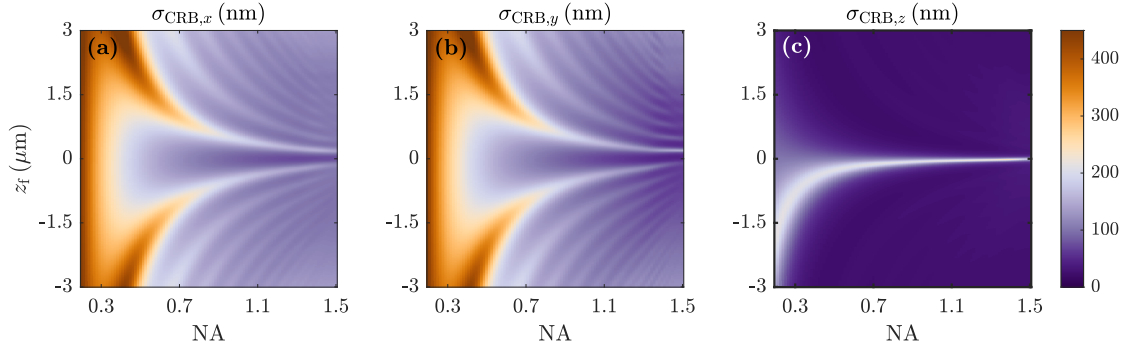


FIG. 2. Cramér-Rao bounds (CRBs) on the standard deviation of 3D localization precision for a gold nanosphere near a glass-water interface at $\theta = 0^\circ$ over a large defocus range and varying numerical aperture (NA). Panels (a–c) show the CRB with respect to the x -, y -, and z -coordinates, respectively. The colorbar represents the value of the CRBs in nm.

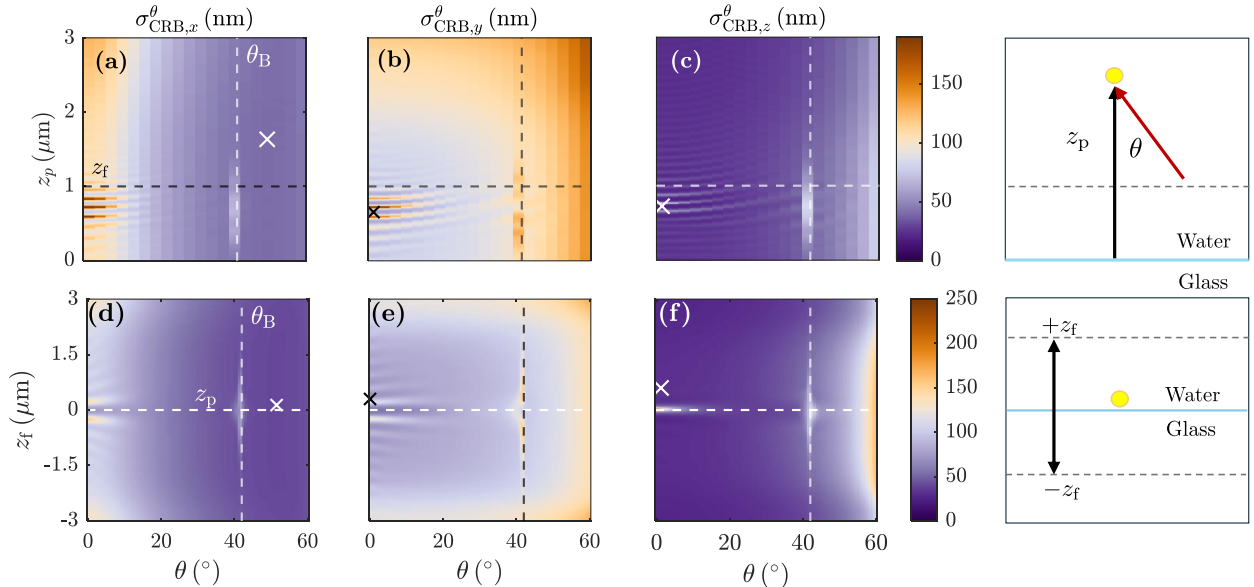


FIG. 3. Cramér-Rao bounds (CRBs) on the standard deviation of 3D localization precision for a gold nanosphere near a glass-water interface under off-axis illumination. In (a–c), results are shown for a fixed focus plane $z_f = 1 \mu\text{m}$ (dashed line), while the particle position z_p is varied from near the interface up to $3 \mu\text{m}$. In (d–f), the particle position z_p is fixed near the interface (dashed line), and z_f is varied over a large defocus range. The vertical dashed lines in panels (a–f) indicate the Brewster angle $\theta_B \approx 42^\circ$. Furthermore, in panels (a–f) the global minimum is denoted by a cross, indicating the best possible bound. Each colorbar represents the CRBs, with values given in nm.

move slightly with z_p but leave the integrated FI nearly constant. Oblique illumination shows a similar behavior: oscillatory structure near the IPSF center but smoother integrated FI, as depicted in Fig. 4(b).

Lastly, we examine whether the improved CRBs under oblique illumination extend to rotating coherent scattering microscopy (ROCS), where oblique illumination is rotated around the optical axis and images are summed incoherently. Figure 4 compares the IPSFs for isCAT (b) and ROCS (c) at $z_f = 500 \text{ nm}$. While ROCS yields a narrower IPSF and thus higher spatial resolution [7, 9], its CRBs for 3D localization ($\sigma_{\text{CRB},\gamma_i}^\theta$) are significantly worse, see

values in panels (b),(c). Incoherent averaging suppresses the outer interference rings, leading to loss of information across all defocus values (panel d). For example, at $\theta = 60^\circ$, $\sigma_{\text{CRB},x}$ in ROCS is more than twice that in isCAT, requiring $\sim 5 \times$ more photons for similar precision. In practice, dense samples complicate this trade-off: uncontrolled interference degrades isCAT precision, while ROCS is more robust under such conditions.

Discussion.—We have discussed 3D localization precision in interferometric microscopy with oblique illumination. Based on a precise classical and quantum FI computation, we find that oblique illumination can increase

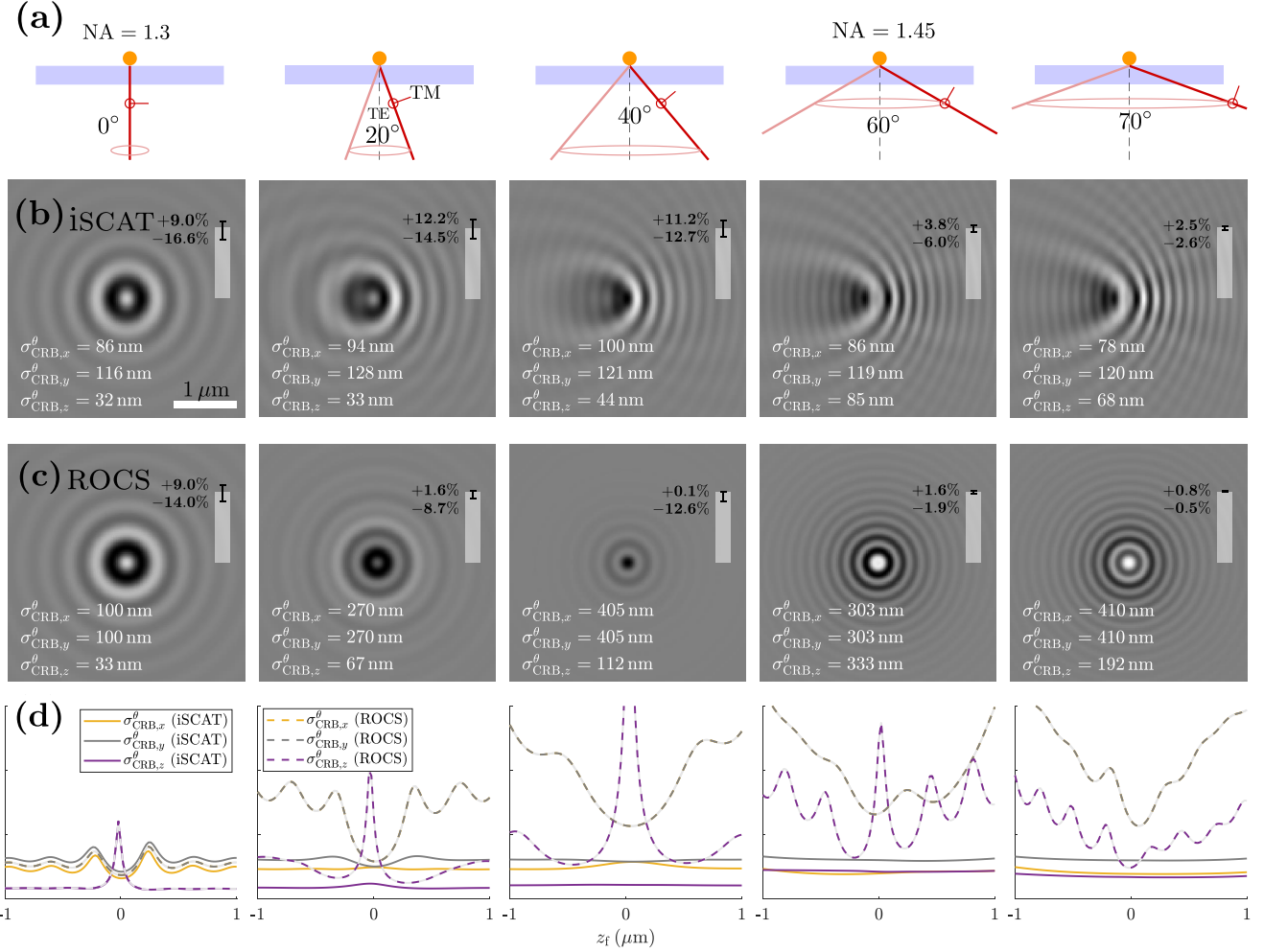


FIG. 4. Interferometric scattering microscopy (iSCAT) and rotating coherent scattering microscopy (ROCS) images for a gold nanosphere on top of a glass substrate. (a) We consider an incoming plane wave with TE polarization and the different angles reported in the insets. (b) iSCAT images for a focus position of $z_f = 500$ nm. (c) Corresponding ROCS images, which we obtain by rotating the incoming wave around the z -axis and summing (incoherently) over the resulting iSCAT images. The Cramér-Rao bounds (CRBs) obtained from the iSCAT and ROCS images are reported in the respective panels, where σ_x corresponds to $\sigma_{\text{CRB},x}^{\theta}$ with corresponding assignments for y and z . (d) The CRBs as a function of defocus show that the localization precision in ROCS is consistently worse than in oblique iSCAT. Since the CRBs for x and y in ROCS are identical, they are represented by a single gray dashed line.

both the transverse and axial localization precision by roughly a factor of two. The framework of FI flow provides an intuitive explanation for this phenomenon and also visualizes the dependence of the achievable localization precision on the system's NA.

When comparing iSCAT and ROCS imaging modalities, we find that ROCS provides worse localization precision, despite its higher spatial resolution. Interestingly, both the higher spatial resolution and the worsening of the localization precision have their origin in the incoherent integration of images from different illumination directions. A similarly counterintuitive result is found for iSCAT with Brewster angle illumination. Here, the contrast improves [13], but the CRBs for localization preci-

sion worsen. These examples show that resolution and contrast alone are not sufficient to fully describe the performance of an imaging modality.

Our results on QCRBs can be generalized to any imaging scheme based on coherent scattering. The observed increase in localization precision could benefit various applications, from classical iSCAT to plasmonics [23], nanoparticle cooling and trapping [24], and the imaging of ultracold atoms [25].

This project has received funding from the European Research Council (ERC) under the European Union's Horizon 2020 research and innovation program (Grant Agreement No. 758752) and the Swiss National Science Foundation (Grant PZ00P2_216211). The authors

acknowledge the financial support by the University of Graz. The authors declare no competing interests. Data underlying the results presented in this paper are not publicly available at this time but may be obtained from the authors upon reasonable request.

* Contact author: felix.hitzelhammer@uni-graz.at

- [1] G. Young, N. Hundt, D. Cole, A. Fineberg, J. Andrecka, A. Tyler, A. Olerinyova, A. Ansari, E. G. Marklund, M. P. Collier, S. A. Chandler, O. Tkachenko, J. Allen, M. Crispin, N. Billington, Y. Takagi, J. R. Sellers, C. Eichmann, P. Selenko, L. Frey, R. Riek, M. R. Galpin, W. B. Struwe, J. L. P. Benesch, and P. Kukura, *Science* **360**, 423 (2018).
- [2] R. W. Taylor, R. G. Mahmoodabadi, V. Rauschenberger, A. Giessl, A. Schambony, and V. Sandoghdar, *Nat. Photonics* **13**, 480 (2019).
- [3] M. Küppers, D. Albrecht, A. D. Kashkanova, J. Lühr, and V. Sandoghdar, *Nat. Commun.* **14**, 1962 (2023).
- [4] R. W. Taylor and V. Sandoghdar, *Interferometric Scattering (iSCAT) Microscopy and Related Techniques*, in *Label-Free Super-Resolution Microscopy* (Springer International Publishing, 2019) pp. 25–65.
- [5] R. Gholami Mahmoodabadi, R. W. Taylor, M. Kaller, S. Spindler, M. Mazaheri, K. Kasaiyan, and V. Sandoghdar, *Opt. Express* **28**, 25969 (2020).
- [6] J. Dong, D. Maestre, C. Conrad-Billroth, and T. Juffmann, *J. Phys. D: Appl. Phys.* **54**, 10.1088/1361-6463/ac0f22 (2021).
- [7] D. Ruh, J. Mutschler, M. Michelbach, and A. Rohrbach, *Optica* **5**, 1371 (2018).
- [8] F. Jünger, D. Ruh, D. Strobel, R. Michiels, D. Huber, A. Brandel, J. Madl, A. Gavrilov, M. Mihlan, C. C. Daller, *et al.*, *Nat. Commun.* **13**, 1758 (2022).
- [9] K. Iqbal, J. C. Thiele, E. Pfitzner, and P. Kukura, *ACS Photonics* **12**, 2647 (2025).
- [10] H. V. Trees, Classical detection and estimation theory, in *Detection, Estimation, and Modulation Theory* (John Wiley & Sons, Ltd, 2001) Chap. 2, pp. 19–165.
- [11] M. P. Backlund, Y. Shechtman, and R. L. Walsworth, *Phys. Rev. Lett.* **121**, 023904 (2018).
- [12] D. Bouchet, S. Rotter, and A. P. Mosk, *Nat. Phys.* **17**, 564 (2021).
- [13] F. Hitzelhammer, A. Dostálová, I. Zykov, B. Platzer, C. Conrad-Billroth, T. Juffmann, and U. Hohenester, *ACS Photonics* **11**, 2745 (2024).
- [14] J. Hüpf, F. Russo, L. M. Rachbauer, D. Bouchet, J. Lu, U. Kuhl, and S. Rotter, *Nat. Phys.* **20**, 1294 (2024).
- [15] N. S. Ginsberg, C.-L. Hsieh, P. Kukura, M. Piliarik, and V. Sandoghdar, *Nat Rev Methods Primers* **5**, 23 (2025).
- [16] U. Hohenester, N. Reichelt, and G. Unger, *Comp. Phys. Commun.* **276**, 108337 (2022).
- [17] U. Hohenester, *Comp. Phys. Commun.* **294**, 108949 (2024).
- [18] Y. Liu, V. Stergiopoulou, J. Chuah, M. Unser, D. Sage, and J. Dong, arXiv preprint arXiv:2502.03170 (2025).
- [19] L. Novotny and B. Hecht, *Principles of Nano-Optics*, 2nd ed. (Cambridge University Press, 2012).
- [20] Y. Shechtman, S. J. Sahl, A. S. Backer, and W. E. Moerner, *Phys. Rev. Lett.* **113**, 133902 (2014).
- [21] J. Chao, E. S. Ward, and R. J. Ober, *J. Opt. Soc. Am. A* **33**, B36 (2016).
- [22] T. Juffmann, S. Nimmrichter, F. Balzarotti, and J. Dong, *Photoniques* **131**, 58 (2025).
- [23] M. Schmid, P. Andrae, and P. Manley, *Nanoscale Res. Lett.* **9**, 50 (2014).
- [24] C. Gonzalez-Ballester, M. Aspelmeyer, L. Novotny, R. Quidant, and O. Romero-Isart, *Science* **374**, eabg3027 (2021).
- [25] W. Ketterle, D. S. Durfee, and D. M. Stamper-Kurn, *IOS press* **140**, 67 (1999).
- [26] P. B. Johnson and R.-W. Christy, *Phys. Rev. B* **6**, 4370 (1972).

END MATTER

Figure. 5 shows (Q)CRBs on the 3D localization precision for a gold nanosphere near a glass-air interface. Panel (a) shows improved localization precision along the x -axis but reduced precision along the y -axis. We note that the z -localization precision for a gold nanosphere at a glass-air interface benefits from off-axis illumination Figs. 3(c) and (d)], whereas this is not the case at a glass-water interface [Figs. 3(c) and (f)]. For a glass-air interface [Fig. 5(d)], the QCRBs follow the same trends as for a glass-water interface [Fig. 1(d)], with the difference that the glass-air interface yields lower values for z -localization precision. In Fig. 6, we plot the best achieved

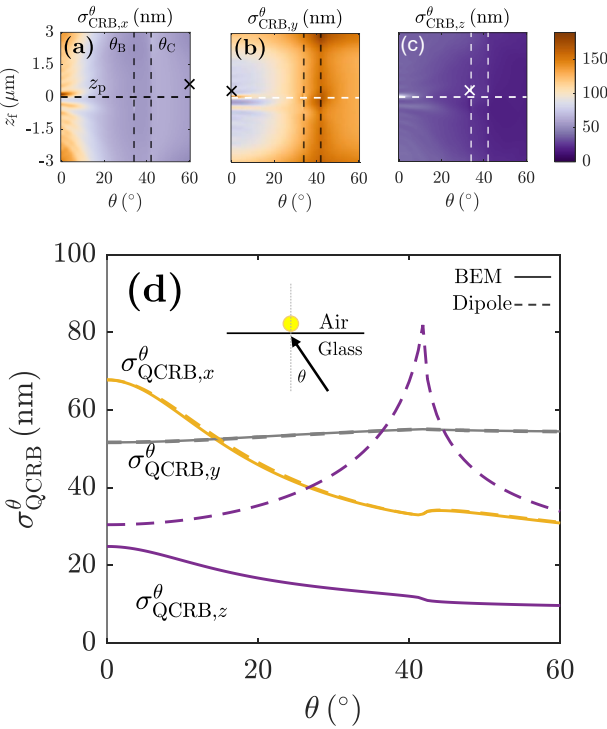


FIG. 5. (Quantum) Cramér-Rao bounds on the standard deviation of 3D localization precision for a gold nanosphere at a glass-air interface under off-axis illumination. In (a–c), the particle position z_p is fixed near the interface, while the defocus plane is varied over a large range. Dashed lines indicate the Brewster angle, $\theta_B \approx 34^\circ$, and the critical angle, $\theta_C \approx 42^\circ$. Additionally, in panels (a–c) the global minimum is denoted by a cross, indicating the best possible bound. In (d), the dependence of the QCRBs on the illumination angle for the glass-air interface is shown. The colorbar represents CRB values in nanometers.

able bound under off-axis illumination-denoted by the crosses in Figs. 3(d),(f) and 5(a),(c), against the CRBs

obtained for on-axis illumination. For the simulations, the following parameters were chosen: a gold sphere; excitation wavelength in vacuum $\lambda = 520$ nm; numerical

Table I. Comparison of on- and off-axis quantum Cramér-Rao bounds for 3D localization precision. We take the minimum $\min_{\theta \in I_\theta} [\sigma_{QCRB}^\theta]$ achieved under off-axis illumination. The right-most column shows the enhancement factor g .

Interface	σ_{QCRB}^θ on-axis	$\min [\sigma_{QCRB}^\theta]$ off-axis	Gain
Glass-water	$\sigma_{QCRB,x}^\theta = 69$ nm	$\min [\sigma_{QCRB,x}^\theta] = 25$ nm	$g \approx 2.8$
Glass-water	$\sigma_{QCRB,z}^\theta = 23$ nm	$\min [\sigma_{QCRB,z}^\theta] = 23$ nm	$g \approx 1$
Glass-air	$\sigma_{QCRB,x}^\theta = 68$ nm	$\min [\sigma_{QCRB,x}^\theta] = 31$ nm	$g \approx 2.2$
Glass-air	$\sigma_{QCRB,z}^\theta = 25$ nm	$\min [\sigma_{QCRB,z}^\theta] = 10$ nm	$g \approx 2.5$

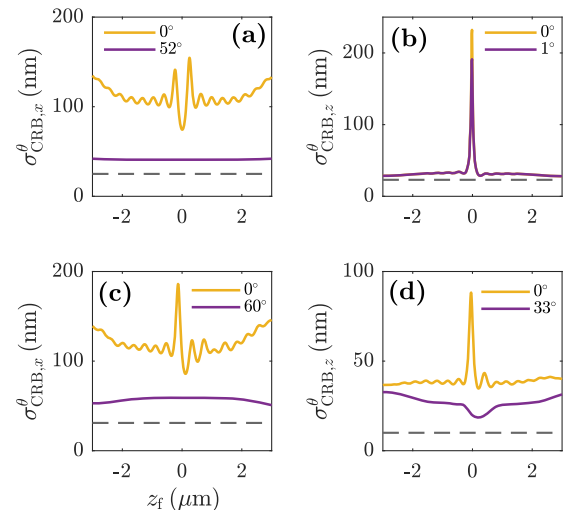


FIG. 6. Comparison of the Cramér-Rao bounds (CRBs) for localization precision under on-axis illumination (yellow line) and the lowest achievable bounds under off-axis illumination (purple line) over a large defocus range. The dashed gray lines indicate the minimum QCRBs obtained under off-axis illumination, with numerical values listed in Table I. Panels (a) and (b) correspond to a glass-water interface, and panels (c) and (d) to a glass-air interface, where in each case the global minima (denoted by \times in Figs. 3 and 5) are used for the purple line.

aperture NA = 1.3; linear x -polarization of the incoming light; particle diameter of 30 nm (only in Fig. 1(a–c) the diameter is 50 nm); for cases where the particle is placed near the interface, the particle-interface distance is set to 1 nm; refractive index of glass $n = 1.5$; and depending on the setup, a refractive index of $n = 1$ (air) or $n = 1.33$ (water). The field of view (FOV) is $4 \times 4, \mu\text{m}$ with 152 pixels. The material parameters for gold are taken from [26].